Journal of Materials Chemistry A

ROYAL SOCIETY OF CHEMISTRY

PAPER

View Article Online
View Journal | View Issue

Cite this: J. Mater. Chem. A, 2025, 13, 5415

Amorphous-like thermal conductivity and high thermoelectric figure of merit in "π" SnS and SnSe†

Min Zhang, [a] Ioanna Pallikara,[ab] Joseph M. Flitcroft [a] and Jonathan M. Skelton *[a]

Received 19th August 2024
Accepted 2nd January 2025

DOI: 10.1039/d4ta05815a

rsc.li/materials-a

We present a detailed first-principles characterisation of the thermoelectric performance of the cubic "π" phases of SnS and SnSe. The complex structures push the "particle-like" contribution to the lattice thermal conductivity, κ_{latt}, below the amorphous limit, resulting in an ultra-low κ_{latt} from room temperature upwards. The cubic symmetry supports larger Seebeck coefficients than the orthorhombic phases, but higher carrier effective masses and stronger electron scattering require high doping levels to optimise the conductivity and power factors. For π SnSe, we predict a low-temperature n-type figure of merit, *ZT*, comparable to Bi_2Te_3, and a high-temperature *ZT* competitive with the flagship orthorhombic SnSe. These results demonstrate the exceptional promise of these systems as high-performance thermoelectrics, and highlight structural complexity as a route to optimising low-temperature *ZT* by minimising the κ_{latt}.

1 Introduction

With over half of global energy wasted as heat,[1,2] practical heat recovery is critical from both an environmental and economic standpoint. Thermoelectric (TE) power directly converts heat to electricity through the Seebeck effect in a TE material, with potential applications to energy harvesting and for improving energy efficiency at multiple scales.[2] The performance of a TE material is expressed by the dimensionless figure of merit *ZT*:[2,3]

$$ZT = \frac{S^2\sigma T}{\kappa_{el} + \kappa_{latt}} \quad (1)$$

where S is the Seebeck coefficient, σ is the electrical conductivity, $S^2\sigma$ is the power factor (PF), and κ_{el} and κ_{latt} are the electronic and lattice (phonon) components of the thermal conductivity κ. S, σ and κ_{el} are related through the carrier concentration n, which can be controlled by chemical doping and is typically optimised in heavily-doped semiconductors.[3] κ_{latt} is independent of the electronic transport and must be minimised to achieve a high *ZT*. Typical materials engineering strategies to optimise *ZT* include doping and alloying, which can both improve the electrical properties, for example by increasing n or modulating the electronic structure to induce "band convergence", and/or can reduce the κ_{latt}.[4–8]

A variety of materials have been studied as prospective TEs including chalcogenides, skutterudites, half-Heuslers, zintl compounds, clathrates, oxides, and oxychalcogenides (ref. 9 and references therein). The current industry-standard materials for low- and high-temperature applications are based on Bi_2Te_3 ($ZT \simeq 1$ from 350–450 K,[2] *ZT* up to 1.9 reported for nanostructured $(Bi_{1-x}Sb_x)Te_3$ alloys[10,11]) and PbTe (*ZT* up to 2.2 at 915 K with endotaxial nanostructuring[12]). However, the low abundance of Te precludes widespread adoption, and thus alternative materials composed of more abundant elements are critical.[2]

The discovery of high *ZT* in orthorhombic SnSe (up to 2.6 in single crystals[13] and 3.1 in polycrystalline samples[14]) has led to considerable interest in the group IV–VI sulphides and selenides. The favourable electrical properties of these materials are well established from the use of SnS as a photovoltaic (PV) absorber material,[15] and SnS and SnSe both show unusually low κ_{latt} associated with the high-temperature *Pnma* → *Cmcm* phase transition.[16–19] However, the "headline" *ZT* in orthorhombic SnSe is only achieved at high temperature, whereas many potential applications require the recovery of low-grade waste heat,[2] and so orthorhombic SnSe cannot replace Bi_2Te_3.

While the thermoelectric performance of orthorhombic SnS and SnSe is well characterised, the IV–VI chalcogenides display a rich structural chemistry, with several potential phases that could show superior low-temperature performance (Fig. 1).[21–23] Among these, the recently-discovered metastable cubic "π" phase of SnS and SnSe[24–26] have shown considerable potential for PV applications.[27–29] A recent study of the IV–VI

[a]Department of Chemistry, University of Manchester, Oxford Road, Manchester M13 9PL, UK. E-mail: jonathan.skelton@manchester.ac.uk

[b]School of Chemical and Process Engineering, University of Leeds, Woodhouse Lane, Leeds LS2 9JT, UK

† Electronic supplementary information (ESI) available: Includes further details of the calculations and analysis performed in this work, and additional data in figures and tables to support the results and discussion. See DOI: https://doi.org/10.1039/d4ta05815a

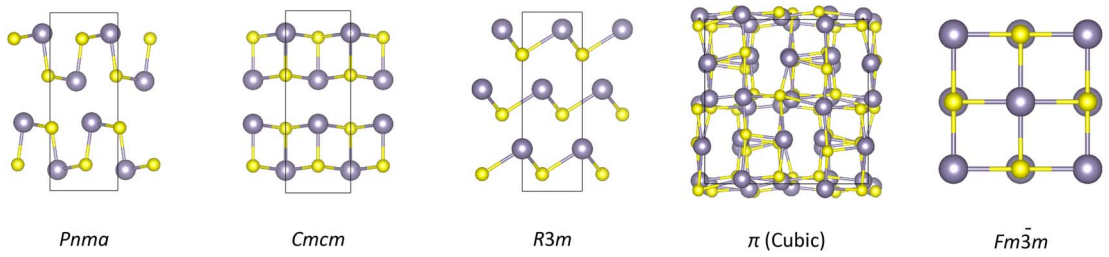

Fig. 1 Structures adopted by the group IV–VI monochalcogenides: orthorhombic *Pnma* and *Cmcm*, rhombohedral *R3m*, and cubic π ($P2_13$) and rocksalt ($Fm\bar{3}m$) phases. These images were prepared using VESTA.[20]

chalcogenides also revealed new structural–property relationships that suggest the π structure should lend itself to low κ_{latt}.[23] The potential thermoelectric performance of the π phases has been explored in several computational studies,[30–32] but significant approximations in the calculations mean the results are at best indicative.

We have developed a fully *ab inito* workflow for predicting *ZT*, by combining state-of-the-art approaches to computing the *S*, σ, κ_{el} and κ_{latt},[33–35] which we and others have validated against multiple classes of TE materials including chalcogenides,[36,37] oxides[38–40] and oxychalcogenides.[41,42] In this study, we apply this workflow to obtain high-quality reference predictions of the thermoelectric performance of π SnS and SnSe. π SnS and SnSe have lower κ_{latt} and higher (absolute) *S* than the corresponding orthorhombic phases, but at the cost of higher carrier effective masses, stronger electron scattering, and lower σ, which requires heavier doping to offset. The majority of the κ_{latt} occurs through intraband tunnelling characteristic of amorphous materials,[43,44] leading to very low thermal conductivity at and above room temperature. With n-type doping at the level achieved in experiments on p-type SnS and SnSe,[45,46] π SnSe has a low-temperature *ZT* comparable to Bi_2Te_3 and a high-*T ZT* competitive with orthorhombic SnSe, resulting in a large average *ZT* for low- to mid-temperature applications. More generally, these findings highlight targeting structural complexity as a viable strategy for suppressing the low-*T* κ_{latt} in TE materials to optimise the *ZT* toward more widespread heat-recovery applications.

2 Computational methods

Calculations were performed using plane-wave density-functional theory (DFT) as implemented in the Vienna *Ab initio* Simulation Package (VASP) code.[47] Initial structures of π SnS and SnSe were taken from previous work[22] and optimised to tight tolerances of 10^{-8} eV on the total energy and 10^{-2} eV Å^{-1} on the forces. PBEsol+D3 (ref. 48 and 49) was used to describe electron exchange and correlation, as this has been shown to provide an accurate description of the structure and dynamics of these materials.[21] Projector-augmented wave (PAW) pseudopotentials[50,51] were used to describe the ion cores, with the valence configurations: Sn – $5s^25p^2$, S – $3s^23p^4$, and Se – $4s^24p^4$. A plane-wave basis with a kinetic-energy cutoff of 600 eV was employed with a 4 × 4 × 4 *Γ*-centred Monkhorst–Pack *k*-point mesh[52] to model the valence electrons.

Phonon and κ_{latt} calculations were performed using the Phonopy and Phono3py codes.[35,53] The second-order (harmonic) force constants were obtained using a displacement step of 10^{-2} Å and 2 × 2 × 2 supercell expansions with 512 atoms. The third-order (anharmonic) force constants were computed using a step of 3×10^{-2} Å and the 64-atom unit cells. Phonon dispersion curves were obtained by interpolating the frequencies along *q*-point paths between the high-symmetry points in the $P2_13$ Brillouin zone. Atom-projected density of states (PDoS) curves were obtained from frequencies evaluated on uniform *Γ*-centered *q*-point grids with 24 × 24 × 24 subdivisions. The "particle-like" contribution to the κ_{latt} was determined by solving the phonon Boltzmann transport equation (BTE) within the single-mode relaxation-time approximation (SM-RTA), using modal properties computed on 10 × 10 × 10 *Γ*-centered *q*-point grids. Testing on smaller 8 × 8 × 8 meshes confirmed the SM-RTA and full linarised BTE solution[54] are quantitatively similar (Fig. S1, ESI†). The "wave-like" intraband tunnelling contribution to the κ_{latt} was additionally obtained by solving the Wigner transport equation.[43,44]

The *S*, σ and κ_{el} were determined by solving the electron BTE within the momentum relaxation-time approximation (MRTA) as implemented in the AMSET code.[34] Accurate electronic bandgaps, E_g, and uniform band structures were obtained using non-self-consistent HSE06.[55,56] Energy- and momentum-dependent electron relaxation times were estimated from the rates of acoustic deformation potential (ADP), ionized impurity (IMP), piezoelectric (PIE), and polar optical phonon (POP) scattering.[34] The deformation potentials were determined from single-point calculations on deformed structures generated with AMSET. The elastic constant matrices *C*, high-frequency/static dielectric constants $\varepsilon_\infty/\varepsilon_S$, Born effective-charge tensors Z^* and piezoelectric tensors $e^{(0)}$ were obtained using the finite differences and density-functional perturbation theory (DFPT) approaches in VASP.[57,58] All properties were computed with PBEsol+D3 apart from the ε_∞, which were computed using non-self-consistent HSE06. The POP frequencies ω_{po} were calculated by combining the phonon frequencies at $q = \Gamma$ from Phonopy with the Z^* from DFPT.[58] *k*-point convergence tests and validation of non-self-consistent HSE06 are provided in Table S1.†

Finally, defect calculations were performed to investigate potential dopants for the π phases, requiring additional

calculations on a set of reference elemental metals and metal chalcogenides/halides and a series of *Pnma* and π SnS and SnSe models with atomic substitutions. A list of reference systems, and the chosen *k*-point meshes, are provided in Table S2.†

Additional details of the calculations and analysis performed in this work, including key equations, are provided in Section 1 of the ESI.†

3 Results and discussion

3.1 Structure, dynamics and lattice thermal conductivity

The structural chemistry of the Group IV–VI oxides and chalcogenides is strongly influenced by the stereochemical activity of the valence ns^2 lone pair on the tetrel T^{2+} cations. This gives rise to five structure types across the TCh series (T = Ge/Sn/Pb, Ch = S/Se/Te), *viz.* a high-symmetry cubic rocksalt phase ($Fm\bar{3}m$ spacegroup), two low-symmetry orthorhombic phases (*Pnma*, *Cmcm*), and intermediate-symmetry rhombohedral and cubic π phases ($R3m$/$P2_13$) (Fig. 1).

The heavier PbCh form the rocksalt structure, in which the Pb^{2+} cations adopt a centrosymmetric octahedral environment with six equal Pb–Ch bond lengths and the $6s^2$ lone pairs are inactive. For GeS/GeSe and SnS/SnSe, the "strain" induced by placing the Ge^{2+}/Sn^{2+} in a centrosymmetric environment leads to an energetic preference for the orthorhombic *Pnma* structure, where the "pseudo-2D" layered structure and three-coordinate geometry allow the $4s^2$/$5s^2$ lone pairs to project into an interlayer void space. The $R3m$ phase adopted by GeTe, and by SnTe at low temperature, lies between these extremes, with a cation off-centering along the rocksalt {111} direction giving three short and three long T–Te bonds and a partial relaxation of the strain in the higher-symmetry phase.

The π structure is a distorted 2 × 2 × 2 expansion of the eight-atom rocksalt conventional cell, and differs significantly from the rhombohedral phase in that it retains a cubic $P2_13$ spacegroup but with a larger primitive cell with $n_a = 64$ atoms. The *Pnma* structure has one unique Sn site with one short and two long bonds to chalcogen atoms (Table S3†). In contrast, the π structure has four Sn sites, with 2 × 4 atoms in rhombohedral-like sites with three equivalent Sn–Ch distances and the other 2 × 12 in sites with three different Sn–Ch bond lengths.

We predict optimised lattice constants of $a = 11.38$ and 11.77 Å for π SnS and SnSe, respectively, which are within 2% of the measured $a = 11.6$ and 11.97 Å.[24,26] Previous studies have shown that both π phases are dynamically stable (*i.e.* there are no imaginary modes in the phonon dispersion curves) and energetically metastable with respect to the orthorhombic phases of SnS and the orthorhombic and rocksalt phases of SnSe.[21,22,31,59] Our calculated phonon spectra confirm the dynamical stability, with real frequencies across the Brillouin zone (Fig. 2 and S2†).

Using the SM-RTA we predict room-temperature κ_{latt} from "particle-like" transport, κ_p, of 0.26 and 0.18 W m^{-1} K^{-1} for π SnS and SnSe. These are well below the averaged values of 0.96–5.01 W m^{-1} K^{-1} for IV–VI chalcogenides in the other structure types in Fig. 1 obtained from similar calculations.[23] We previously showed that low κ_{latt} in the IV–VI chalcogenides arises from a balance of low phonon group velocities and a large "phase space" of energy- and momentum-conserving phonon scattering pathways, favoured by structure types with large primitive cells, and strong three-phonon interactions, favoured in structures where the T^{2+} are constrained to locally-symmetric environments.[23] Separating the κ_p into harmonic (group velocity) and weighted-average lifetime components, κ/τ^{CRTA} and τ^{CRTA}, confirms the large unit cell of the π structure reduces the group velocities by ∼75–80% compared to the *Pnma* phases (Fig. 3(a)). The τ^{CRTA} of π SnS and SnSe are also around 30 and 50% smaller above 300 K (Fig. 3(b)). We stress that we only use the CRTA model to determine a weighted-average lifetime to compare materials, and we do not use this approximation to calculate the κ_{latt}. Comparison of the "phase space" functions $\bar{N}2(\omega)$ indicate that the π phases show comparable numbers of scattering pathways to the *Pnma* phases, but with higher spectral weight at low frequency (Fig. 3(c)). This does not follow the

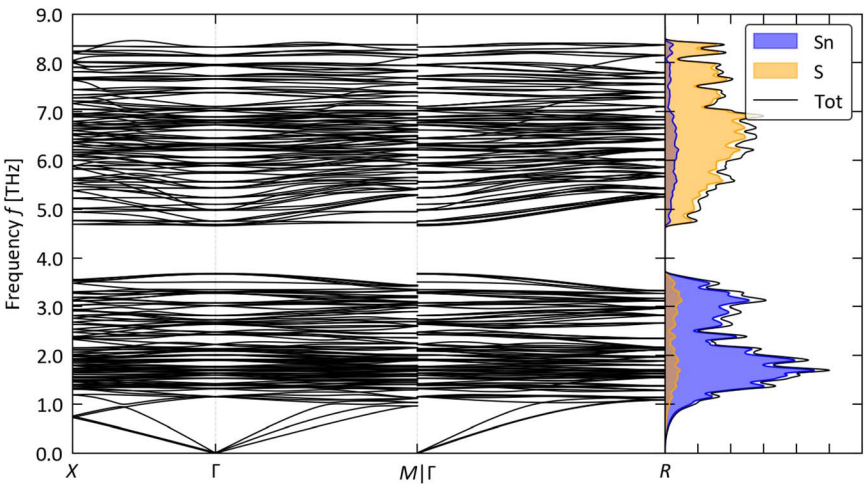

Fig. 2 Phonon dispersion and density of states (DoS) of π SnS. The blue and orange shaded regions show the projections of the DoS onto the Sn and S atoms, respectively.

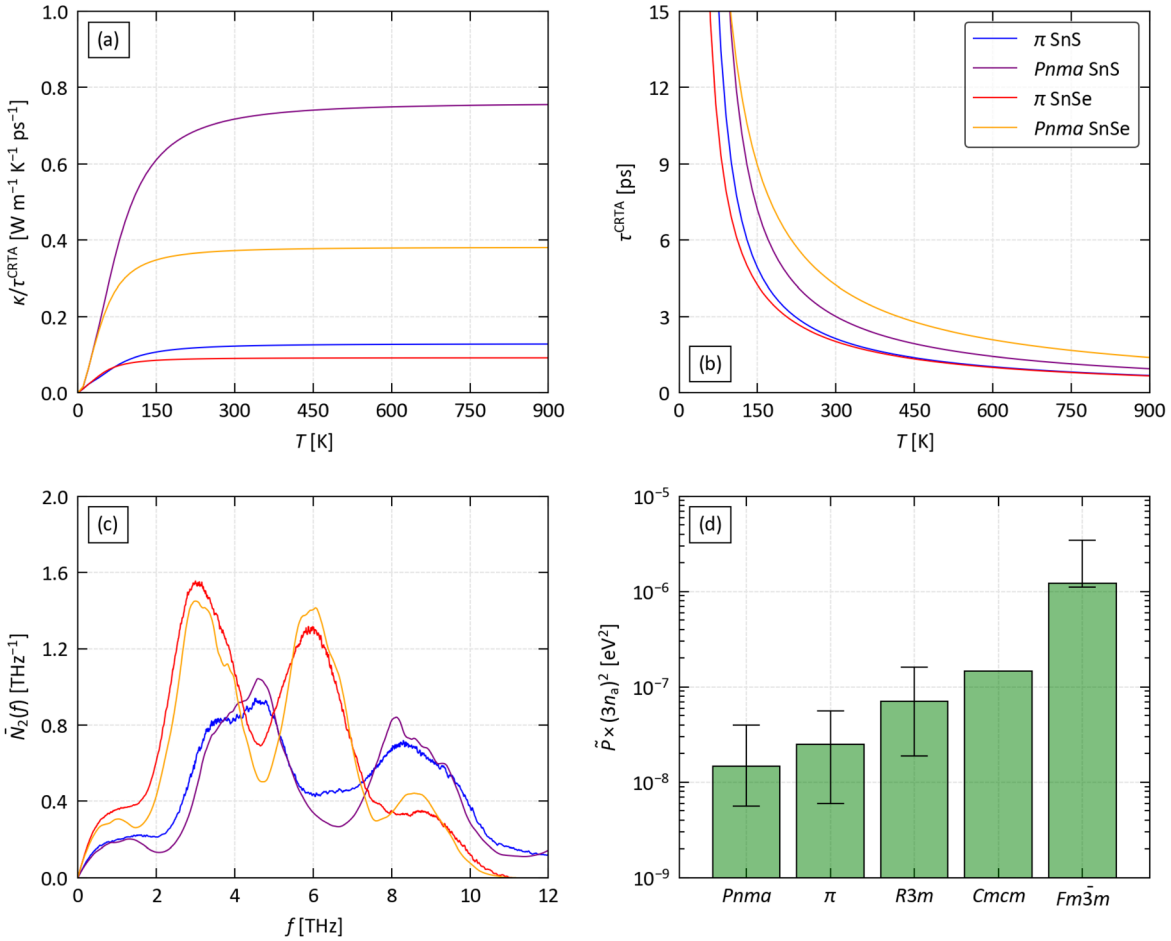

Fig. 3 Analysis of the "particle-like" thermal conductivity, κ_p, of π SnS and SnSe using the models employed in our previous studies.[23,60,61] (a)/(b) Separation of the scalar average κ_p into a harmonic term κ/τ^{CRTA} (a) and weighted-average lifetime τ^{CRTA} (b). The κ/τ^{CRTA} and τ^{CRTA} are indicative of differences in the phonon group velocities and lifetimes, respectively. (c) Scaled average number of energy- and momentum-conserving three-phonon scattering channels ("phase space", $\bar{N}_2$) as a function of frequency. (d) Weighted-average three-phonon interaction strengths $\tilde{P}$ compared to other IV–VI chalcogenides, including *Pnma* SnS and Ge/Sn selenides and tellurides in the crystal phases shown in Fig. 1. Where applicable, ranges are indicated by error bars. The data for *Pnma* SnS and SnSe in (a)–(c) are taken from our previous work.[61] The $\tilde{P}$ in (d) are taken from our previous study,[23] but include the $\tilde{P}$ for *Pnma* SnS from ref. 61.

trend with unit-cell size in our previous study,[23] indicating that the larger numbers of energy-conserving scattering channels potentially enabled by the denser phonon dispersions may be offset by momentum conservation restrictions from the higher cubic symmetry. The calculated $\tilde{P}$ place the anharmonicity in the π phases between the *Pnma* and *R*3*m* phases (Fig. 3(d)), which can be ascribed to 25% of the Sn atoms being in more constrained rhombohedral-like environments (*cf.* Table S3†).

The dense phonon dispersions result in very small intraband spacing (*cf.* Fig. 2), which, combined with the short lifetimes, suggests "wave-like" heat transport through intraband tunnelling, characteristic of amorphous materials, is likely to be significant.[43,44] The condition suggested in ref. 44 is:

$$\Delta f_{ave} \leq \frac{f_{max}}{3n_a} \quad (2)$$

where Δf_{ave} is the average intraband spacing and f_{max} is the maximum frequency in the dispersion. This condition is close to being met in both π SnS ($\Delta f_{ave} = 4.4 \times 10^{-2}$ THz, $f_{max}/(3n_a) =$ 4×10^{-2} THz) and SnSe (2.9×10^{-2} THz, 2.5×10^{-2} THz). Fig. 4(a) shows the contributions of the RTA κ_p and intraband tunnelling κ_w, obtained by solving the Wigner transport equation,[43,44] to the κ_{latt} of π SnSe. The κ_p and κ_w become equal around 200 K and the κ_w accounts for 78% of the κ_{latt} at 700 K. In contrast, the κ_w of *Pnma* SnSe is almost negligible at 300 K and increases the κ_{latt} by 18% at 700 K (Fig. S3†). π and *Pnma* SnS show similar, contrasting, behaviour (Fig. S4/S5†). The very low κ_p confirms the strategy of targeting large, complex unit cells can reduce the κ_p below the amorphous limit.[23] A consequence of the shallow temperature dependence of the κ_w is that π SnS and SnSe have 70–75% lower thermal conductivity than the *Pnma* phases at 300 K, and κ_{latt} comparable to the layering *b* direction in the orthorhombic structures, which is the "hard" axis for thermal transport,[61] at high T (Fig. 4(b)).

To the best of our knowledge the κ_{latt} of π SnS and SnSe have not been measured. We previously predicted a room-temperature lattice thermal conductivity of 0.13 W m^{-1} K^{-1} for π SnS.[62] However, this calculation did not account for intraband

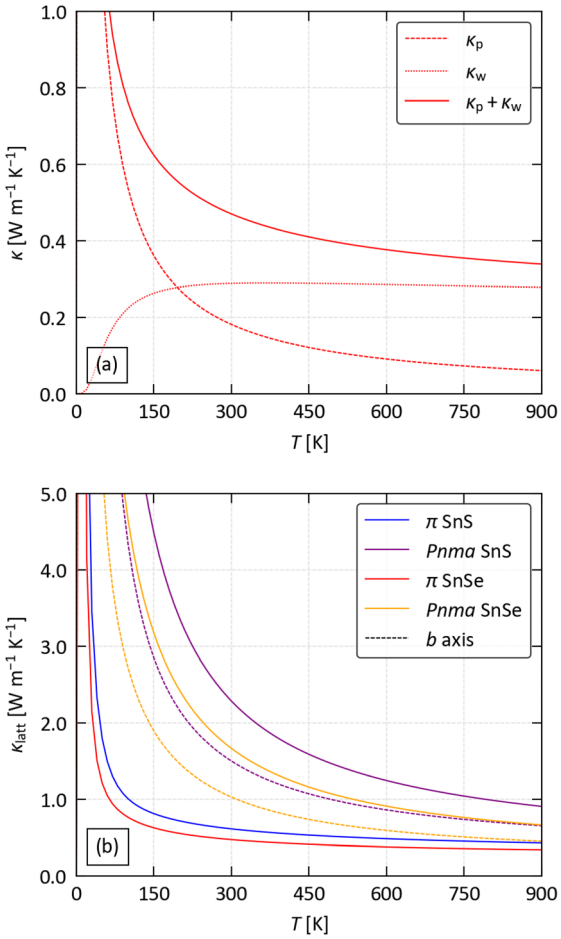

Fig. 4 Lattice thermal conductivity κ_{latt} of π SnS and SnSe. (a) Contribution of "particle-like" and "wave-like" transport κ_p/κ_w to the total κ_{latt} of π SnSe. (b) Comparison of the scalar average κ_{latt} of π SnS and SnSe to the orthorhombic *Pnma* phases. For the two *Pnma* phases, we show both the orientationally-averaged κ_{latt} (solid lines) and the κ_{latt} along the layering direction (crystallographic *b* axis; dashed lines). Data for the *Pnma* phases were taken from our previous work[61] and the κ_{latt} were recalculated to include the κ_w contribution.

tunneling and is equivalent to the κ_p obtained in the present study. Using the data from ref. 62, we obtain a κ_w of 0.32 W m^{-1} K^{-1} and a total κ_{latt} of 0.45 W m^{-1} K^{-1} (Fig. S6†), which is 26% lower than predicted in the present work. One possible explanation for this discrepancy is the use of a dispersion correction in the present calculations, which has a small but noticeable effect on the phonon dispersion (Fig. S7†).[61] This can be ascribed to the ∼3.3% smaller equilibrium volume predicted with the dispersion correction, since the phonon frequencies, and, by extension, κ_{latt}, can be highly sensitive to the volume.[63]

Related to this point, the anharmonicity in the π phases could indicate large thermal expansion, which could have a significant impact on the κ_{latt}. Using the quasi-harmonic phonon calculations in our previous work,[22] we estimate volume expansions of 4.1 and 4.3%, relative to the athermal equilibrium volume, V_0, for π SnS and SnSe, respectively, at T = 900 K (Fig. S8†). Given the large cost of computing the third-order force constants, it is not feasible to perform "full" κ_{latt} calculations at these expanded cell volumes. Instead, we adopt the approximate model used in our previous work,[61,64] and combine harmonic phonon calculations at 3.5/6.6 and 3.4/6.5% expanded volumes of π SnS and SnSe, respectively, from the calculations in ref. 22 with the $\tilde{P}$ obtained at V=V_0 in the present work (see Section 1.4 of the ESI†). This method accounts for the effect of thermal expansion on the phonon group velocities and three-phonon scattering phase space, under the assumption that the average three-phonon interaction strengths are similar to those at the equilibrium volume. Expansion of the unit cell leads to a reduction in the phonon frequencies and, consequently, the κ_{latt} (Fig. S9–S12†). With a ∼3.5% expanded volume, we predict a reduction in κ_{latt} of around 13% at T = 900 K (24% at a larger ∼6.5% expanded volume), due mostly to a reduction in the κ_w (Fig. S11/S12†). We therefore conclude that thermal expansion may have a moderate impact on the κ_{latt} of the π phases, and that our predicted κ_{latt} at high T is likely to be overestimated. For π SnS, we predict that a 3.5% volume expansion will reduce the κ_{latt} by 18% at 300 K, which suggests that differences in the predicted V_0 largely do account for the discrepancy between the present work and our previous calculation.[62]

Other computational studies[31,32] predicted room-temperature κ_{latt} of 5.15 and 2.54/0.86 W m^{-1} K^{-1} for π SnS and SnSe using the Slack model,[65] but the larger predictions suggest this model is likely not appropriate for these systems. On the other hand, ref. 31 predicted thermal conductivities of 0.49 and 0.32 W m^{-1} K^{-1} for π SnS and SnSe using the Cahill model for the minimum thermal conductivity,[66] which are remarkably similar to the present calculations.

3.2 Electrical transport

The calculated electronic band structures and DoS of π SnS and SnSe (Fig. S13†) are comparable to previous studies[67,68] and yield direct bandgaps of E_g = 1.61 and 1.28 eV that are an excellent match to experimental measurements[25,26] and previous calculations.[31,67] The σ, S and κ_{el} of the π phases were calculated as a function of temperature and an extrinsic carrier concentration n ("doping level") by solving the electron BTE[33] with energy- and momentum-dependent electron scattering rates from four scattering processes common to semiconductors.[34] With this approach, we estimate per-state electron lifetimes, which is an improvement on previous computational studies that have determined the σ and κ_{el} with respect to an unknown, fixed or state-independent relaxation times.[30–32]

The doping level is a key parameter for optimising the electrical properties of semiconductor thermoelectrics.[3] *Pnma* SnS and SnSe can be both p-type (hole) and n-type (electron) doped[14,15,45,69–72] at n up to 5 × 10^{19} cm^{-3}.[45,46,71] Fig. 5 shows the predicted σ, absolute $|S|$, PF $S^2\sigma$ and κ_{el} of the π and *Pnma*[36,37] phases of SnS and SnSe, for p- and n-type doping with n = 10^{16}–10^{20} cm^{-3} and T = 700 K. This temperature was chosen to be well below the high-temperature *Pnma* → *Cmcm* phase transitions in orthorhombic SnS and SnSe (T = 878/807 K[73]).

The π phases are predicted to have 10–20× lower σ with p-type doping, and ∼10× lower σ with n-type doping, than their

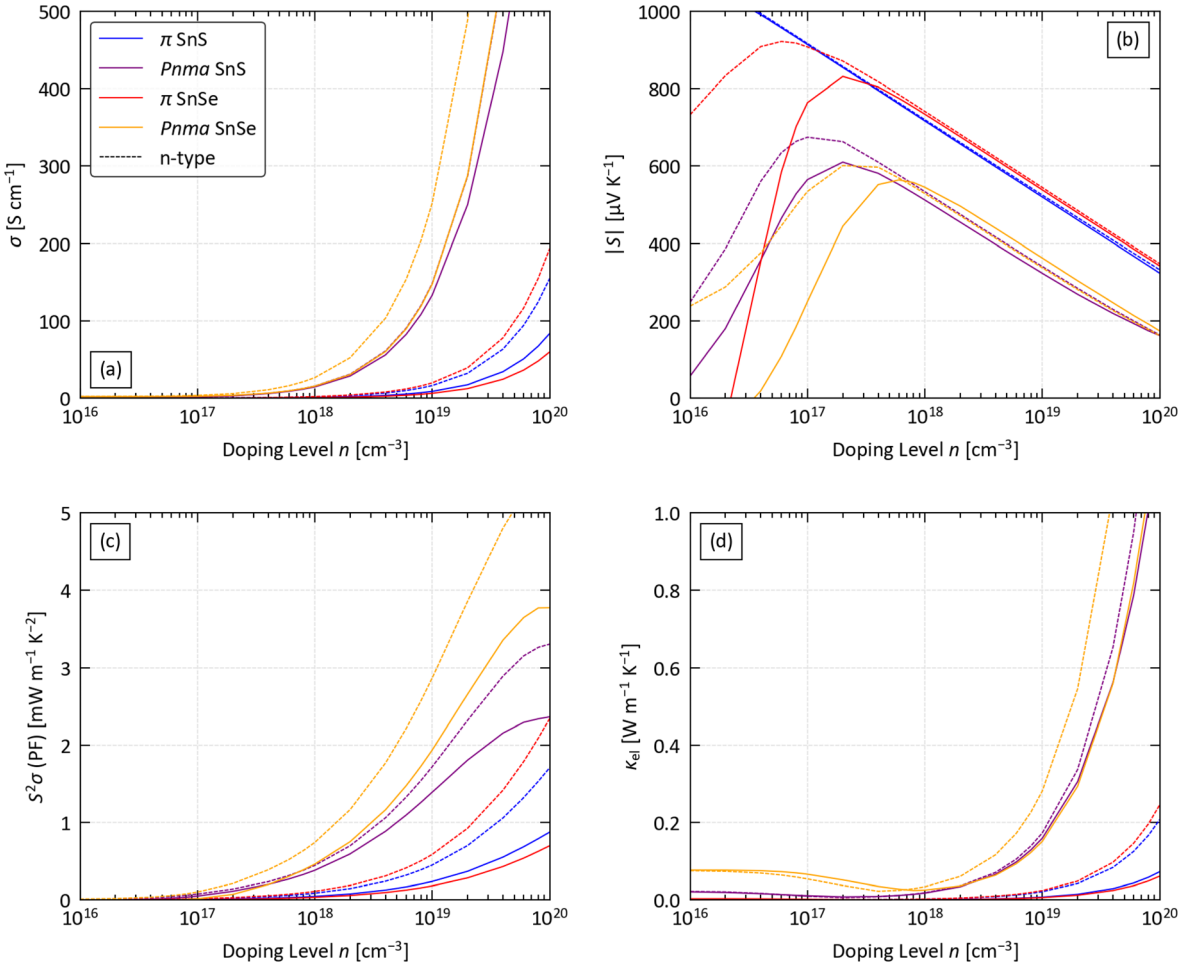

Fig. 5 Predicted electrical properties of π SnS and SnSe as a function of extrinsic carrier concentration n ("doping level") at $T = 700$ K: (a) electrical conductivity σ, (b) absolute Seebeck coefficient $|S|$, (c) power factor $S^2\sigma$ (PF), and (d) electronic thermal conductivity κ_{el}. Data for p- and n-type doping are shown by solid and dashed lines respectively. Predicted orientationally-averaged properties for *Pnma* SnS and SnSe taken from our previous studies[36,37] are shown for comparison.

Pnma counterparts (Fig. 5(a)). This is partially offset by a 1.5–2× larger $|S|$ (Fig. 5(b)), but the net result is that the *Pnma* phases have up to 8× larger PFs at a reference $n = 4 \times 10^{19}$ cm^{-3}. As for the *Pnma* phases,[37] we predict larger σ but comparable $|S|$ with n-type doping, yielding reasonable PFs of 1.1 and 1.4 mW m^{-1} K^{-2} for π SnS and SnSe, respectively, that can be enhanced to 1.7 and 2.3 mW m^{-1} K^{-2} at a larger $n = 10^{20}$ cm^{-3} (Fig. 5(c)). On the other hand, at higher n the κ_{el} are proportional to the σ through the Wiedemann–Franz law,

$$\kappa_{el} = L\sigma T \tag{3}$$

where L is the Lorentz number, which in general is not constant. We predict a negligible κ_{el} of <0.1 W m^{-1} K^{-1} for the π phases with $n = 4 \times 10^{19}$ cm^{-3} compared to ~1 W m^{-1} K^{-1} for n-type *Pnma* SnSe under the same conditions. This analysis shows that optimising the electrical properties of the π phases requires n-type doping at a level comparable to, or ideally higher than, the highest p-type doping levels reported in experiments on *Pnma* SnSe.[45,46]

The electrical conductivity is given by:

$$\sigma = ne\mu = ne \times \frac{(e\tau)}{m_\sigma^*} \tag{4}$$

where e is the elementary charge and μ is the carrier mobility, determined by the lifetime τ and conductivity effective mass m_σ^*, obtained from a weighted average over the bands that contribute to the transport. The Seebeck coefficient is related to the Seebeck effective mass m_S^* and n according to:[3]

$$S = \frac{8\pi^2 k_B^2}{3qh^2} m_S^* \left(\frac{\pi}{3n}\right)^{2/3} \tag{5}$$

where $q = \pm e$ for hole and electron carriers, respectively, h is the Planck constant and k_B is the Boltzmann constant. The m_σ^* and m_S^* for the *Pnma* and π phases of SnS and SnSe were determined according to the procedure in ref. 74 at a nominal $n = 4 \times 10^{19}$ cm^{-1} and $T = 700$ K, and are presented in Table S4.† We calculate m_σ^* between 1.1–2.5 m_e for the π phases, which are ~5–10× larger than the corresponding 0.15–0.27 m_e for the *Pnma* phases. On the other hand, the m_S^* of the π phases are 3–

4× larger than those of the *Pnma* phases. These differences partially account for the lower conductivity and higher Seebeck coefficients of the π phases. Furthermore, the m^*_σ for electrons are around 30 and 45–50% lower than holes in the *Pnma* and π phases, respectively, whereas the m^*_S differ by <10%, which explains the larger predicted n-type conductivity and power factors.

The m^*_σ and m^*_S can be used to calculate the Fermi surface complexity factor $(N^*_V K^*)$, where N^*_V is the effective valley degeneracy, *i.e.* the number of band extrema involved in the transport, and K^* is the effective anisotropy factor that describes the shape of the carrier pockets in the Fermi surface.[74] The $(N^*_V K^*)$ shows a strong correlation to the maximum power factor, and values above ∼10 are characteristic of materials such as the lead chalcogenides where features of the electronic structure are known to contribute significantly to the thermoelectric performance.[74–76] We calculate $(N^*_V K^*) = 4.6/5.1$ for p-type *Pnma* SnS/SnSe and 8.2/11 for the n-type materials, while the larger m^*_σ of the π phases result in 60–80% smaller values of 1.1/1.7 and 3.2/3.7. This implies that the electronic structures of the *Pnma* phases show features that are beneficial for the thermoelectric properties, and that these features are largely absent in the π phases. While we do not calculate the N_V or K explicitly, the values of $(N^*_V K^*) = 1.1 - 3.7$ predicted for the π phases suggest either a low effective valley degeneracy and/or an effective anisotropy $K < 1$.

Furthermore, comparing the carrier mobilities as a function of n indicates the μ are also an order of magnitude lower in the π phases (Fig. S14/S15†). The μ of both the *Pnma* and π phases is limited by polar-optic phonon (POP) scattering[36,37] (Fig. S14–S17†), for which the scattering rates are proportional to the POP frequency ω_{po} and inversely proportional to the high-frequency and static dielectric constants $\varepsilon_\infty/\varepsilon_S$.[34,77] The π phases have larger ω_{po} and smaller ε, which both favour stronger scattering. The lower σ of the π phases can therefore be explained both by larger carrier masses, as discussed above, and stronger (POP) carrier scattering.

The temperature dependence of the electrical properties is typically secondary to doping level. At the larger n required to obtain reasonable PFs, the $S^2\sigma$ of the π phases decrease with temperature due to a metallic-like decrease in σ typical of heavily-doped ("degenerate") semiconductors (Fig. S18/S19†). As in the *Pnma* phases, this is partially offset by an increase in the $|S|$,[36,37] but for n-type π-SnSe there is a ∼30% reduction in the PF, from ∼2 to 1.4 mW m^{-1} K^{-2}, between 300–700 K at our reference $n = 4 \times 10^{19}$ cm^{-3}.

There have been a limited number of experimental studies on the π phases for photovoltaic applications. Measurements on thin films of n-type π SnS yielded a conductivity of 0.1 S cm^{-1} at 673 K and $n = 3.7 \times 10^{17}$ cm^{-3},[78] which is comparable to our predicted 0.7 S cm^{-1}. Similarly, measurements on $Sn(S_{0.45}Se_{0.55})$ films obtained a p-type conductivity of 2×10^{-2} S cm^{-1} at 723 K and $n = 10^{16}$ cm^{-3},[79] which falls between our predicted $\sigma = 0.9 \times 10^{-2}$ and 6×10^{-2} S cm^{-1} for π SnS and SnSe. Nair *et al.* reported that the room-temperature σ of *Pnma* SnS and SnSe are 2–3 orders of magnitude larger than the corresponding π phases,[28] which is qualitatively consistent with our findings. The Seebeck coefficients of 485 and 314 μV K^{-1} measured for p-type SnS–SnSe and SnS–SnSe–SnS stacks, with $n = 9 \times 10^{15}$ and 10^{15} cm^{-3} respectively,[80] are less than half the maximum we predict. Our calculations on both π structures suggest the S change sign with temperature at low n, which could account for this discrepancy (Fig. S18/S19†).

We predict Seebeck coefficients of $|S| \simeq 300$–600 μV K^{-1} at carrier concentrations between 10^{19}–10^{20} cm^{-3}, which are similar to the calculations in ref. 31. However, the electron lifetimes in ref. 31 were calculated from the deformation potential, and do not account for the dominant POP scattering, so the predicted conductivity is significantly larger than in the present study. Our predictions of higher σ and PFs with n-type doping are also qualitatively consistent with the "reduced" values from the calculations in ref. 30.

3.3 Thermoelectric figure of merit

Combining the S, σ, κ_{el} and κ_{latt} allows us to predict the figure of merit ZT as a function of doping level and temperature (eqn (1)) For n-type π SnSe, an industrially-viable $ZT > 1$ can be obtained at T as low as 300 K, and $ZT \simeq 3$, comparable to state-of-the-art experiments on orthorhombic SnSe,[14] can be obtained at high temperature (Fig. 6(b)). With $n = 4 \times 10^{19}$ cm^{-3} we predict maximum ZT, ZT_{max}, of 1.6 and 2.4 for n-type π SnS and SnSe, respectively, close to the orthorhombic *Pnma* → *Cmcm* transition temperatures of 878 and 800 K[73] (Table S4†). These are larger than the ZT_{max} of the p-type *Pnma* phases predicted by similar calculations, and very similar to the n-type ZT_{max} (Table S4†).[36,37] Larger $n = 10^{20}$ cm^{-3} improve the limiting electrical conductivity and PFs of the π phases, yielding significantly improved ZT_{max} of 2.2 and 3. Both the *Pnma* and π phases are predicted to show superior performance with n-type doping,[37] but the differences are much larger in the π phases, with p-type $ZT > 1$ only attainable at high T and large n (Fig. S20 and Table S5†).

Previous theoretical studies have predicted p-type ZT of 0.83 and 1.2 for π SnS and SnSe, respectively, at 800 K[31] and ZT between 0.74 and 1 between 300–900 K for π SnSe.[30,32] At the same $T = 800$ K and $n = 10^{20}$ cm^{-3} employed in ref. 31, we predict larger p-type $ZT = 1.21$ and comparable $ZT = 1.25$ for π SnS and SnSe. This study also predicted higher $S^2\sigma$ with p-type doping, in contrast to our results, which is likely due to the neglect of POP scattering when calculating the σ as noted above. The calculated ZT in ref. 30 are obtained by neglecting the κ_{latt} entirely, while ref. 32 estimates the κ_{latt} with the Slack model and uses a constant electron relaxation time to calculate the σ and κ_{el}, all of which are likely to be poor approximations. However, since neither study specifies the carrier concentration(s) at which the ZT were calculated, it is impossible to compare to our calculations.

While many flagship thermoelectrics perform best at high temperature, the majority of applications require good low-T performance.[2] We predict π SnSe to have $ZT = 1.1$ and 1.3 at 300 K, with $n = 4 \times 10^{19}$ and 10^{20} cm^{-3}, respectively, which are ∼2–3× larger than p-type *Pnma* SnSe (Fig. 7(a)). The "device efficiency" η of a thermoelectric generator is given by:[2]

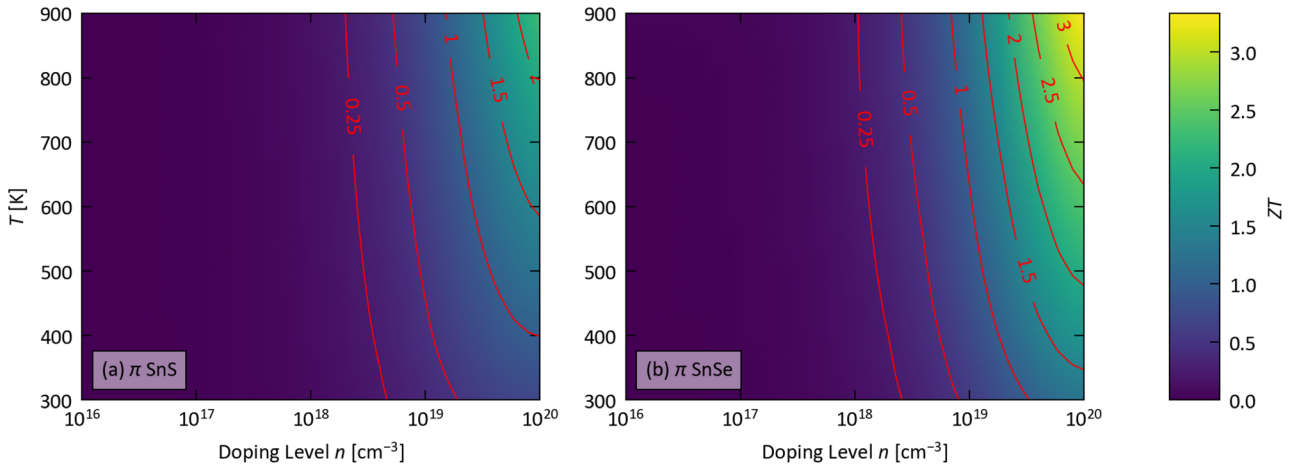

Fig. 6 Predicted thermoelectric figure of merit ZT of n-type π SnS (a) and SnSe (b) as a function of extrinsic electron carrier concentration n ("doping level") and temperature T. Values of ZT = 0.25, 0.5, 1, 1.5, 2, 2.5, and 3 are shown by contour lines.

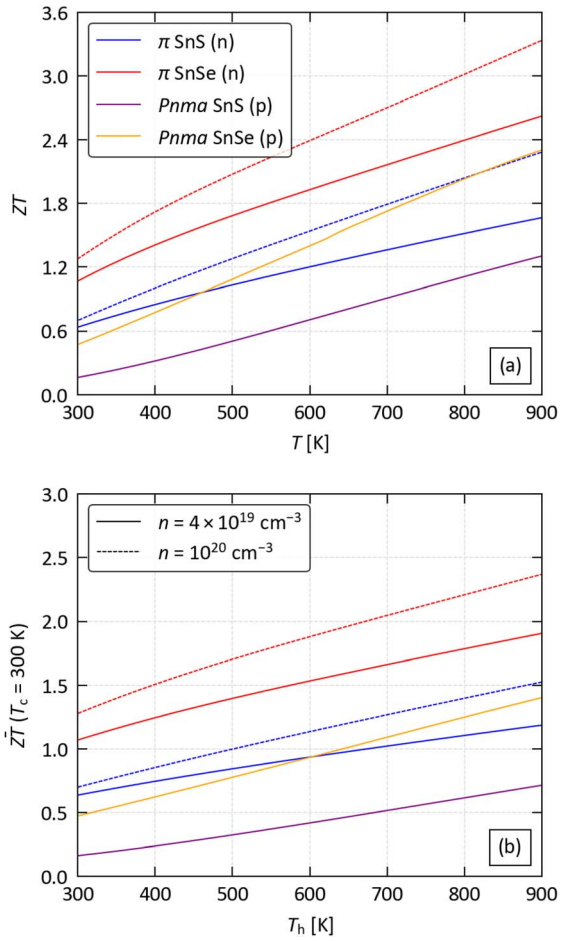

Fig. 7 Thermoelectric efficiency of n-type π SnS and SnSe. (a) Figure of merit ZT as a function of temperature. (b) Average figure of merit $\overline{ZT}$ as a function of the hot-side temperature T_h with a cold-side temperature T_c = 300 K. Solid and dashed lines show the predicted $ZT/\overline{ZT}$ obtained at doping levels of $n = 4 \times 10^{19}$ and 10^{20} cm^{-3} respectively. The predicted orientationally-averaged $ZT/\overline{ZT}$ of p-type *Pnma* SnS and SnSe with $n = 4 \times 10^{19}$ cm^{-3} are shown for comparison. These data were taken from our previous studies,[36,37] but the lattice thermal conductivities κ_{latt} were recalculated to include the intraband tunnelling contribution κ_w.

$$\eta = \frac{T_h - T_c}{T_h}\left(\frac{\sqrt{1+\overline{ZT}}-1}{\sqrt{1+\overline{ZT}}+\frac{T_c}{T_h}}\right) \quad (6)$$

where T_h and T_c are the hot- and cold-side temperatures, respectively, and $\overline{ZT}$ is the average ZT for the p- and n-type couple over the temperature range $T_c \rightarrow T_h$. The continuous increase in the ZT with temperature results in a $\overline{ZT}$ that increases continuously up to ~1.9 and 2.3 at T_h = 800 K with the two doping levels (Fig. 7(b)). In contrast, the slower rise in ZT with temperature in *Pnma* SnSe means $\overline{ZT} > 1$ is only achieved when $T_h \geq$ 650 K. Our results therefore show that n-type π SnSe, given a suitable doping level, could display viable thermoelectric performance for a wide range of low-to-mid temperature applications.

A similar contrast is seen between π and *Pnma* SnS, *i.e.* the π phase performs better at low T and therefore shows a higher $\overline{ZT}$ over a wide temperature range. However, the generally lower ZT means the threshold of $\overline{ZT} = 1$ is not reached until T_h = 675 K (500 K with $n = 10^{20}$ cm^{-3}). However, for larger T_h = 880 K we predict reasonable $\overline{ZT}$ of 1.2 and 1.5 at the two doping levels. For applications where sulphide-based TEs are preferred, exploring doping strategies to maximise the n of π SnS may therefore be facile.

In order to realise our predictions experimentally, the key challenges of synthesising and stabilising the π phases, and optimising the electrical properties, will need to be addressed. π SnS and SnSe have been prepared in nanoparticulate and thin-film form with a variety of techniques including chemical bath deposition (CBD),[81] solution synthesis,[25,82] spray pyrolysis,[83,84] and aerosol-assisted chemical vapour deposition (AACVD).[85] A number of experiments have examined thermal stability, with the consensus that π SnS transforms to the *Pnma* phase on heating to around 600 K or higher.[82,84,85] If the stability "window" cannot be widened, π SnS and SnSe could only be used for low-temperature applications.

The structural preferences of the IV–VI chalcogenides can be understood in terms of the stereochemical activity of the tetrel lone pair, which is driven by the interaction between the tetrel and chalcogen atoms.[86] Generally, the lighter chalcogenides prefer lower-symmetry phases (*e.g.* SnS/SnSe and GeS/GeSe adopt the orthorhombic *Pnma* phase), while heavier chalcogenides prefer higher-symmetry phases (*e.g.* SnTe, GeTe and the Pb chalcogenides adopt the rhombohedral and rocksalt phases). Previous studies have found that π SnS is closer to the convex hull than π SnSe ($\Delta G = 2.3$ and 3 kJ per mol per F.U. at 300 K).[21,22,68] The existence of a direct conversion pathway to the orthorhombic phase has not, to our knowledge, been established, but we have previously considered conversion to the structurally-similar rocksalt phases and obtained energy barriers of 8.5 and 2.2 kJ per mol F.U. for π SnS and SnSe.[22] Based on this, admittedly incomplete, information, we suggest that the π phases might be stabilised by elements that favour the *Pnma*/*R*3*m*-like local geometry over the six-coordinate geometry in the rocksalt phases. This suggests that a SnS/SnSe solid solution could be used to stabilise π SnSe, or that alloying with GeS or GeSe could be used to stabilise the π phases of both Sn chalcogenides.

Literature on the relevant properties of the π phases is currently sparse, and the largest n-type carrier concentrations of 4×10^{17} reported to date[78] are orders of magnitude lower than we predict are required to achieve high thermoelectric performance. p-type orthorhombic SnS and SnSe have been prepared with n up to 4×10^{19} cm^{-3},[45,46] and experiments on n-doped SnSe have reported comparable n up to 5×10^{19} cm^{-3}.[71] Established dopants for the *Pnma* phases include Na and Ag (p-type),[45,46,64] and the halogens Cl and Br (n-type).[15,87–89] Several studies have also investigated Sb and Bi as potential n-type dopants, with reported n up to $\sim 4 \times 10^{19}$ cm^{-3}.[90,91]

To determine whether these six dopants might be used to optimise the carrier concentrations of the π phases, we performed a series of calculations to compare the doping energies E_d for substitution into *Pnma* and π SnS/SnSe (Section 1.6 and Table S6, ESI†). For p-type doping, we predict a negative E_d for Na at the concentrations of ~3 at% in our models, due to the relative instability of elemental Na, whereas we predict E_d of 1.3–1.5 eV for Ag. The negative E_d for Na is likely due to our not having considered all possible competing phases, but the contrast between the predicted E_d of Na and Ag is nonetheless qualitatively consistent with experiments, where large p-type n have been obtained with Na doping[45,46] but a recent study of Ag-doped SnS found that high doping levels of up to 2.78 at% led to segregation of an Ag_2SnS_3 secondary phase.[64] For Cl and Br we predict E_d of 1.5–1.7 and 1.4–1.7 eV, respectively, which compare to values of 0.8–1.1 and 0.6–0.9 eV for Sb and Bi. This suggests that n-type doping by metal substitution at the Sn site may be more facile than halide substitution at the chalcogen site. The calculations predict that all six dopants should fully ionise and not form localised defect levels (Table S6 and Fig. S21–S24†). We note, however, that experiments have shown that Sb can act as an amphoteric dopant,[92] with substitution at both the cation and anion sites (Sb^{3+}/Sb^{3-}), and the present calculations do not account for possible substitution at the chalcogen site. It is also unclear whether Bi may show similar amphoteric behaviour.

We predict similar E_d for Na and Ag in SnS and SnSe, but notably higher E_d for the majority of the electron donors in SnS, which suggests that SnSe can be more easily n-type doped. Excluding Na, for which we predict negative E_d for all four materials, we predict 5 and 16% larger E_d for Ag in π SnS and SnSe, respectively, compared to the *Pnma* phases, and 3–20% larger E_d for the four n-type dopants. This suggests the π phases may be slightly more difficult to dope than their *Pnma* counterparts, but otherwise have similar defect chemistry, as might be expected given the similar local structures. To further assess the stability of the metal dopants, we calculated the precipitation energies E_p for exsolution of the metal chalcogenide in the presence of a chalcogen reservoir (Table S6†). With the exception of the E_p for Na_2S/Na_2Se from *Pnma* SnS and SnSe, which are 70 and 30 meV, respectively, the E_p are negative, indicating that large concentrations of the dopants may not be accommodated unless kinetically trapped. Finally, as a basic "sanity check" on our values, we also compared the formation energies E_f for the metal chalcogenides, including *Pnma* SnS and SnSe, to both the Materials Project calculations[93,94] and to experimental data where available[95–101] (Table S7†). We find generally good agreement, which provides some level of confidence in our predicted E_d/E_p.

Based on our analysis, we tentatively suggest that it should be possible to dope π SnS and SnSe to achieve at least $n \approx 5 \times 10^{19}$ cm^{-3} using Na as a p-type dopant and Sb or Bi as n-type dopants. However, a comprehensive analysis of the defect chemistry should include intrinsic defects, in particular Sn vacancies, and different charge states. A further consideration is also the impact of doping on the (meta)stability of the π phases, since the generally higher E_d could provide an additional driving force for conversion to the *Pnma* phase. However, since the π phases are likely to be kinetically formed and trapped, the effect of the dopants on the kinetics of formation and/or the energy barrier to conversion to other phases may be more important considerations. We defer a more comprehensive exploration of these issues to a future study.

4 Conclusions

This work has provided detailed *ab inito* reference predictions of the transport properties and thermoelectric figure of merit of π SnS and SnSe.

As predicted by a previous analysis of the lattice thermal conductivity of the IV–VI chalcogenides, the complex structure lowers the particle-like transport below the amorphous limit, and the shallow temperature dependence of the intraband tunnelling transport leads to κ_{latt} much lower than other chalcogenides at room temperature, and κ_{latt} competitive with that along the layering direction in the orthorhombic phases at high T. The cubic structures support larger absolute Seebeck coefficients than the *Pnma* phases, but larger carrier effective masses and stronger polar-optic phonon scattering lead to low conductivity, and n-type doping with carrier concentrations on the order of 4×10^{19} cm^{-3}, and ideally larger, are required to

obtain reasonable power factors. If this is achievable, we predict that π SnSe could show $ZT > 1$, competitive with Bi_2Te_3,[9] at room temperature, and ZT as high as 3 at 800 K, matching state-of-the-art experiments on *Pnma* SnSe.[14] With a typical 300 K cold-side temperature, this strong low-temperature performance results in a much higher average ZT than we predict for p-type *Pnma* SnSe, making π SnSe suitable for a wide range of low- to mid-temperature applications. The predicted performance of π SnS is also considerably better than p-type *Pnma* SnS, such that a $\overline{ZT} > 1$ could be achieved for mid-temperature applications if the n can be optimised.

Despite being discovered almost a decade ago, the potential TE performance of the π monochalcogenides has not yet been uncovered, due to a combination of experiments focusing on photovoltaic applications and computational predictions using unsuitable approximations.[30–32] Among the latter, there are likely few circumstances where neglecting the κ_{latt} in the ZT equation would be reasonable.[30] The Slack model significantly overestimates the κ_{latt} of the π phases compared to solving the Wigner transport equation, although the Cahill model works remarkably well.[31] Finally, unless a reasonable estimate of an electron relaxation time can be obtained (*e.g.* from experiments[102,103]), our results suggest electronic transport calculations within the constant relaxation-time approximation cannot be relied upon for quantitative predictions.[32] On the other hand, the good match between our predicted σ and experimental measurements suggests phenomenological models for the electron scattering may be adequate provided they capture the dominant scattering mechanism(s) (POP scattering for *Pnma* and π SnS/SnSe).

While there are potential challenges around stabilising and heavily doping the π phases, in our view the exceptional predicted TE performance, and in particular the ultra-low κ_{latt}, warrants further investigation. On the last point, this study evidences the successful strategy of targeting structural complexity as a route to achieving low room-temperature κ_{latt} and high low-temperature ZT. If our understanding of the IV–VI chalcogenides generalises to the related group IV oxides and V–VI sesquioxides/sesquichalcogenides, further investigation of the low-symmetry orthorhombic phases of the Sb_2Ch_3 and Bi_2Ch_3, or ternary IV–V oxides in the pyrochlore and derived structure types,[38] could be rewarding.

Data availability

Raw data from this study will be made available to download free of charge after publication from an online repository at **https://doi.org/10.17632/6j4vvf5py4**. Our analysis code is available on GitHub at **https://github.com/skelton-group/ZT-Calc-Workflow**.

Author contributions

Conceptualisation – JMS; methodology – all authors; data curation – all authors; formal analysis and investigation – all authors; writing (original draft) – all authors; writing (review and editing) – all authors; funding acquisition – JMS. All authors have read and agreed to the published version of the paper.

Conflicts of interest

There are no conflicts to declare.

Acknowledgements

MZ is supported by a CSC studentship (202006700004). JMS and JMF are supported by a UK Research and Innovation Future Leaders Fellowship (MR/T043121/1, MR/Y033973/1), and JMS previously held a University of Manchester Presidential Fellowship. This work used the ARCHER2 UK National Supercomputing Service *via* the UK Mateirals Chemistry Consortium (Engineering and Physical Sciences Research Council EP/R029431 and EP/X035859).

Notes and references

1 A. Firth, B. Zhang and A. Yang, *Appl. Energy*, 2019, **235**, 1314–1334.
2 R. Freer and A. V. Powell, *J. Mater. Chem. C*, 2020, **8**, 441–463.
3 G. Tan, L.-D. Zhao and M. G. Kanatzidis, *Chem. Rev.*, 2016, **116**, 12123–12149.
4 Y. Takagiwa, Y. Pei, G. Pomrehn and G. Snyder, *Appl. Phys. Lett.*, 2012, **101**, 092102.
5 Q. Zhang, H. Wang, W. Liu, H. Wang, B. Yu, Q. Zhang, Z. Tian, G. Ni, S. Lee, K. Esfarjani, *et al.*, *Energy Environ. Sci.*, 2012, **5**, 5246–5251.
6 Y. Pei, Z. M. Gibbs, A. Gloskovskii, B. Balke, W. G. Zeier and G. J. Snyder, *Adv. Energy Mater.*, 2014, **4**, 1400486.
7 J. M. Skelton, *JPhys Energy*, 2020, **2**, 025006.
8 J. Qu, A. Balvanz, S. Baranets, S. Bobev and P. Gorai, *Mater. Horiz.*, 2022, **9**, 720–730.
9 R. Freer, D. Ekren, T. Ghosh, K. Biswas, P. Qiu, S. Wan, L. Chen, S. Han, C. Fu, T. Zhu, A. K. M. A. Shawon, A. Zevalkink, K. Imasato, G. J. Snyder, M. Ozen, K. Saglik, U. Aydemir, R. Cardoso-Gil, E. Svanidze, R. Funahashi, A. V. Powell, S. Mukherjee, S. Tippireddy, P. Vaqueiro, F. Gascoin, T. Kyratsi, P. Sauerschnig and T. Mori, *JPhys Energy*, 2022, **4**, 022002.
10 B. Poudel, Q. Hao, Y. Ma, Y. Lan, A. Minnich, B. Yu, X. Yan, D. Wang, A. Muto, D. Vashaee, X. Chen, J. Liu, M. S. Dresselhaus, G. Chen and Z. Ren, *Science*, 2008, **320**, 634–638.
11 S. I. Kim, K. H. Lee, H. A. Mun, H. S. Kim, S. W. Hwang, J. W. Roh, D. J. Yang, W. H. Shin, X. S. Li, Y. H. Lee, G. J. Snyder and S. W. Kim, *Science*, 2015, **348**, 109–114.
12 K. Biswas, J. He, I. D. Blum, C.-I. Wu, T. P. Hogan, D. N. Seidman, V. P. Dravid and M. G. Kanatzidis, *Nature*, 2012, **489**, 414–418.
13 L.-D. Zhao, S.-H. Lo, Y. Zhang, H. Sun, G. Tan, C. Uher, C. Wolverton, V. P. Dravid and M. G. Kanatzidis, *nature*, 2014, **508**, 373–377.

14 C. Zhou, Y. K. Lee, Y. Yu, S. Byun, Z.-Z. Luo, H. Lee, B. Ge, Y.-L. Lee, X. Chen, J. Y. Lee, *et al.*, *Nat. Mater.*, 2021, **20**, 1378–1384.
15 I. Suzuki, S. Kawanishi, T. Omata and H. Yanagi, *JPhys Energy*, 2022, **4**, 042002.
16 C. W. Li, J. Hong, A. F. May, D. Bansal, S. Chi, T. Hong, G. Ehlers and O. Delaire, *Nat. Phys.*, 2015, **11**, 1063–1069.
17 J. M. Skelton, L. A. Burton, S. C. Parker, A. Walsh, C.-E. Kim, A. Soon, J. Buckeridge, A. A. Sokol, C. R. A. Catlow, A. Togo and I. Tanaka, *Phys. Rev. Lett.*, 2016, **117**, 075502.
18 U. Aseginolaza, R. Bianco, L. Monacelli, L. Paulatto, M. Calandra, F. Mauri, A. Bergara and I. Errea, *Phys. Rev. Lett.*, 2019, **122**, 075901.
19 U. Aseginolaza, R. Bianco, L. Monacelli, L. Paulatto, M. Calandra, F. Mauri, A. Bergara and I. Errea, *Phys. Rev. B*, 2019, **100**, 214307.
20 K. Momma and F. Izumi, *J. Appl. Crystallogr.*, 2011, **44**, 1272–1276.
21 J. M. Skelton, L. A. Burton, F. Oba and A. Walsh, *J. Phys. Chem. C*, 2017, **121**, 6446–6454.
22 I. Pallikara and J. M. Skelton, *Phys. Chem. Chem. Phys.*, 2021, **23**, 19219–19236.
23 S. K. Guillemot, A. Suwardi, N. Kaltsoyannis and J. M. Skelton, *J. Mater. Chem. A*, 2024, **12**, 2932–2948.
24 R. Abutbul, A. Garcia-Angelmo, Z. Burshtein, M. Nair, P. Nair and Y. Golan, *CrystEngComm*, 2016, **18**, 5188–5194.
25 R. E. Abutbul, E. Segev, L. Zeiri, V. Ezersky, G. Makov and Y. Golan, *RSC Adv.*, 2016, **6**, 5848–5855.
26 R. E. Abutbul, E. Segev, S. Samuha, L. Zeiri, V. Ezersky, G. Makov and Y. Golan, *CrystEngComm*, 2016, **18**, 1918–1923.
27 U. Chalapathi, B. Poornaprakash and S.-H. Park, *Sol. Energy*, 2016, **139**, 238–248.
28 P. Nair, A. Garcia-Angelmo and M. Nair, *Phys. Status Solidi A*, 2016, **213**, 170–177.
29 E. Barrios-Salgado, L. A. Rodríguez-Guadarrama, M. L. Ramón García, L. G. Martínez, M. Nair and P. Nair, *Phys. Status Solidi A*, 2017, **214**, 1700036.
30 F. K. Butt, B. U. Haq, S. ur Rehman, R. Ahmed, C. Cao and S. AlFaifi, *J. Alloys Compd.*, 2017, **715**, 438–444.
31 S. U. Rehman, F. K. Butt, Z. Tariq, X. Zhang, J. Zheng, G. Naydenov, B. Ul Haq and C. Li, *Int. J. Energy Res.*, 2021, **45**, 6369–6382.
32 M. A. Sattar, N. Al Bouzieh, M. Benkraouda and N. Amrane, *Beilstein J. Nanotechnol.*, 2021, **12**, 1101–1114.
33 G. K. Madsen, J. Carrete and M. J. Verstraete, *Comput. Phys. Commun.*, 2018, **231**, 140–145.
34 A. M. Ganose, J. Park, A. Faghaninia, R. Woods-Robinson, K. A. Persson and A. Jain, *Nat. Commun.*, 2021, **12**, 2222.
35 A. Togo, L. Chaput and I. Tanaka, *Phys. Rev. B: Condens. Matter Mater. Phys.*, 2015, **91**, 094306.
36 J. M. Flitcroft, I. Pallikara and J. M. Skelton, *Solids*, 2022, **3**, 155–176.
37 M. Zhang, J. M. Flitcroft, S. K. Guillemot and J. M. Skelton, *J. Mater. Chem. C*, 2023, **11**, 14833–14847.
38 W. Rahim, J. M. Skelton and D. O. Scanlon, *J. Mater. Chem. A*, 2020, **8**, 16405–16420.
39 W. Rahim, J. M. Skelton and D. O. Scanlon, *J. Mater. Chem. A*, 2021, **9**, 20417–20435.
40 A. Z. Khan, J. M. Flitcroft and J. M. Skelton, *Adv. Mater.*, 2024, **5**, 652–664.
41 K. Brlec, K. B. Spooner, J. M. Skelton and D. O. Scanlon, *J. Mater. Chem. A*, 2022, **10**, 16813–16824.
42 J. M. Flitcroft, A. Althubiani and J. M. Skelton, *JPhys Energy*, 2024, **6**, 025011.
43 M. Simoncelli, N. Marzari and F. Mauri, *Nat. Phys.*, 2019, **15**, 809–813.
44 M. Simoncelli, N. Marzari and F. Mauri, *Phys. Rev. X*, 2022, **12**, 041011.
45 L.-D. Zhao, G. Tan, S. Hao, J. He, Y. Pei, H. Chi, H. Wang, S. Gong, H. Xu, V. P. Dravid, *et al.*, *Science*, 2016, **351**, 141–144.
46 W. He, D. Wang, J.-F. Dong, Y. Qiu, L. Fu, Y. Feng, Y. Hao, G. Wang, J. Wang, C. Liu, *et al.*, *J. Mater. Chem. A*, 2018, **6**, 10048–10056.
47 G. Kresse and J. Hafner, *Phys. Rev. B: Condens. Matter Mater. Phys.*, 1993, **47**, 558.
48 J. P. Perdew, A. Ruzsinszky, G. I. Csonka, O. A. Vydrov, G. E. Scuseria, L. A. Constantin, X. Zhou and K. Burke, *Phys. Rev. Lett.*, 2008, **100**, 136406.
49 S. Grimme, J. Antony, S. Ehrlich and H. Krieg, *J. Chem. Phys.*, 2010, **132**, 154104.
50 P. E. Blöchl, *Phys. Rev. B: Condens. Matter Mater. Phys.*, 1994, **50**, 17953.
51 G. Kresse and D. Joubert, *Phys. Rev. B: Condens. Matter Mater. Phys.*, 1999, **59**, 1758.
52 H. J. Monkhorst and J. D. Pack, *Phys. Rev. B*, 1976, **13**, 5188.
53 A. Togo and I. Tanaka, *Scr. Mater.*, 2015, **108**, 1–5.
54 L. Chaput, *Phys. Rev. Lett.*, 2013, **110**, 265506.
55 A. V. Krukau, O. A. Vydrov, A. F. Izmaylov and G. E. Scuseria, *J. Chem. Phys.*, 2006, **125**, 224106.
56 J. M. Skelton, D. S. Gunn, S. Metz and S. C. Parker, *J. Chem. Theory Comput.*, 2020, **16**, 3543–3557.
57 S. Baroni and R. Resta, *Phys. Rev. B: Condens. Matter Mater. Phys.*, 1986, **33**, 7017–7021.
58 M. Gajdoš, K. Hummer, G. Kresse, J. Furthmüller and F. Bechstedt, *Phys. Rev. B: Condens. Matter Mater. Phys.*, 2006, **73**, 045112.
59 U. Argaman, R. E. Abutbul, Y. Golan and G. Makov, *Phys. Rev. B*, 2019, **100**, 054104.
60 J. Tang and J. M. Skelton, *J. Phys.: Condens. Matter*, 2021, **33**, 164002.
61 J. M. Skelton, *J. Mater. Chem. C*, 2021, **9**, 11772–11787.
62 J. M. Skelton, L. A. Burton, A. J. Jackson, F. Oba, S. C. Parker and A. Walsh, *Phys. Chem. Chem. Phys.*, 2017, **19**, 12452–12465.
63 J. M. Skelton, D. Tiana, S. C. Parker, A. Togo, I. Tanaka and A. Walsh, *J. Chem. Phys.*, 2015, **143**, 064710.
64 Y. Liu, J. M. Skelton, X. Xia, Y. Zhu, D. J. Lewis and R. Freer, *J. Mater. Chem. C*, 2024, **12**, 508–520.
65 G. A. Slack, *Solid State Phys.*, 1979, **34**, 1–71.
66 D. G. Cahill and R. O. Pohl, *Annu. Rev. Phys. Chem.*, 1988, **39**, 93–121.

67 J. M. Skelton, L. A. Burton, F. Oba and A. Walsh, *APL Mater.*, 2017, **5**, 036101.
68 E. Segev, U. Argaman, R. E. Abutbul, Y. Golan and G. Makov, *CrystEngComm*, 2017, **19**, 1751–1761.
69 X. Shi, Z.-G. Chen, W. Liu, L. Yang, M. Hong, R. Moshwan, L. Huang and J. Zou, *Energy Storage Mater.*, 2018, **10**, 130–138.
70 X. Shi, A. Wu, T. Feng, K. Zheng, W. Liu, Q. Sun, M. Hong, S. T. Pantelides, Z.-G. Chen and J. Zou, *Adv. Energy Mater.*, 2019, **9**, 1803242.
71 S. Chandra, U. Bhat, P. Dutta, A. Bhardwaj, R. Datta and K. Biswas, *Adv. Mater.*, 2022, **34**, 2203725.
72 X. Yang, W.-H. Gu, W.-J. Li, Y.-X. Zhang, J. Feng and Z.-H. Ge, *J. Phys. Chem. Solids*, 2023, **172**, 111077.
73 T. Chattopadhyay, J. Pannetier and H. G. Von Schnering, *J. Phys. Chem. Solids*, 1986, **47**, 879–885.
74 Z. M. Gibbs, F. Ricci, G. Li, H. Zhu, K. Persson, G. Ceder, G. Hautier, A. Jain and G. J. Snyder, *npj Comput. Mater.*, 2017, **3**, 8.
75 W. G. Zeier, A. Zevalkink, Z. M. Gibbs, G. Hautier, M. G. Kanatzidis and G. J. Snyder, *Angew. Chem., Int. Ed.*, 2016, **55**, 6826–6841.
76 M. K. Brod and G. J. Snyder, *J. Mater. Chem. A*, 2021, **9**, 12119–12139.
77 H. Fröhlich, *Adv. Phys.*, 1954, **3**, 325–361.
78 K. Jeganath, N. J. Choudhari, G. S. Pai, A. Rao and Y. Raviprakash, *Mater. Sci. Semicond. Process.*, 2020, **113**, 105050.
79 F. D. B. Sánchez, M. T. S. Nair and P. K. Nair, *Semicond. Sci. Technol.*, 2023, **39**, 015003.
80 E. Barrios-Salgado, L. A. Rodríguez-Guadarrama, A. R. Garcia-Angelmo, J. C. Álvarez, M. Nair and P. Nair, *Thin Solid Films*, 2016, **615**, 415–422.
81 A. Garcia-Angelmo, R. Romano-Trujillo, J. Campos-Álvarez, O. Gomez-Daza, M. Nair and P. Nair, *Phys. Status Solidi A*, 2015, **212**, 2332–2340.
82 J. Breternitz, R. Gunder, H. Hempel, S. Binet, I. Ahmet and S. Schorr, *Inorg. Chem.*, 2017, **56**, 11455–11457.
83 S. Polivtseva, I. O. Acik, A. Katerski, A. Mere, V. Mikli and M. Krunks, *Phys. Status Solidi C*, 2016, **13**, 18–23.
84 S. Polivtseva, A. Katerski, E. Kärber, I. O. Acik, A. Mere, V. Mikli and M. Krunks, *Thin Solid Films*, 2017, **633**, 179–184.
85 M. Guc, J. Andrade-Arvizu, I. Y. Ahmet, F. Oliva, M. Placidi, X. Alcobé, E. Saucedo, A. Pérez-Rodríguez, A. L. Johnson and V. Izquierdo-Roca, *Acta Mater.*, 2020, **183**, 1–10.
86 A. Walsh, D. J. Payne, R. G. Egdell and G. W. Watson, *Chem. Soc. Rev.*, 2011, **40**, 4455–4463.
87 Y. Iguchi, K. Inoue, T. Sugiyama and H. Yanagi, *Inorg. Chem.*, 2018, **57**, 6769–6772.
88 X. Hu, W. He, D. Wang, B. Yuan, Z. Huang and L.-D. Zhao, *Scr. Mater.*, 2019, **170**, 99–105.
89 L. Su, T. Hong, D. Wang, S. Wang, B. Qin, M. Zhang, X. Gao, C. Chang and L.-D. Zhao, *Mater. Today Phys.*, 2021, **20**, 100452.
90 X.-L. Shi, K. Zheng, W.-D. Liu, Y. Wang, Y.-Z. Yang, Z.-G. Chen and J. Zou, *Adv. Energy Mater.*, 2018, **8**, 1800775.
91 A. T. Duong, V. Q. Nguyen, G. Duvjir, V. T. Duong, S. Kwon, J. Y. Song, J. K. Lee, J. E. Lee, S. Park, T. Min, J. Lee, J. Kim and S. Cho, *Nat. Commun.*, 2016, **7**, 13713.
92 C. Yamamoto, X. He, T. Katase, K. Ide, Y. Goto, Y. Mizuguchi, A. Samizo, M. Minohara, S. Ueda, H. Hiramatsu, H. Hosono and T. Kamiya, *Adv. Funct. Mater.*, 2021, **31**, 2008092.
93 A. Jain, G. Hautier, S. P. Ong, C. J. Moore, C. C. Fischer, K. A. Persson and G. Ceder, *Phys. Rev. B: Condens. Matter Mater. Phys.*, 2011, **84**, 045115.
94 A. Jain, S. P. Ong, G. Hautier, W. Chen, W. D. Richards, S. Dacek, S. Cholia, D. Gunter, D. Skinner, G. Ceder and K. A. Persson, *APL Mater.*, 2013, **1**, 011002.
95 A. Glibo, M. Reda, Y. Surace, D. M. Cupid and H. Flandorfer, *J. Alloys Compd.*, 2023, **969**, 172320.
96 R. Colin and J. Drowart, *Trans. Faraday Soc.*, 1964, **60**, 673–683.
97 G. Lindberg, A. Larsson, M. Råberg, D. Boström, R. Backman and A. Nordin, *J. Chem. Therm.*, 2007, **39**, 44–48.
98 T. L. Brundzia and O. J. Klep, *Econ. Geol.*, 1988, **83**, 174–181.
99 P. Scardala, V. Piacente and D. Ferro, *J. Less-Common Met.*, 1990, **162**, 11–21.
100 G. K. Johnson, G. Papatheodorou and C. E. Johnson, *J. Chem. Therm.*, 1981, **13**, 745–754.
101 V. R. Sidorko, L. V. Goncharuk and R. V. Antonenko, *Powder Metall. Met Ceram.*, 2008, **47**, 234–241.
102 Y. Liu, J. M. Skelton, X. Xia, Y. Zhu, D. J. Lewis and R. Freer, *J. Mater. Chem. C*, 2024, **12**, 508–520.
103 Y. Zhu, J. M. Skelton, D. J. Lewis and R. Freer, *JPhys Energy*, 2024, **6**, 025027.

